AFRL-AFOSR-JP-TR-2019-0028

Investigate Target reflection and illumination sensitivity in range gated detection

Anthony Guo Ningqun
MONASH UNIVERSITY

04/11/2019
Final Report

DISTRIBUTION A: Distribution approved for public release.

Air Force Research Laboratory
AF Office Of Scientific Research (AFOSR)/ IOA
Arlington, Virginia 22203
Air Force Materiel Command

REPORT DOCUMENTATION PAGE

Form Approved
OMB No. 0704-0188

1. REPORT DATE *(DD-MM-YYYY)*
11-04-2019

2. REPORT TYPE
Final

3. DATES COVERED *(From - To)*
15 Aug 2016 to 14 Aug 2018

4. TITLE AND SUBTITLE
Investigate Target reflection and illumination sensitivity in range gated detection

5a. CONTRACT NUMBER

5b. GRANT NUMBER
FA2386-16-1-4115

5c. PROGRAM ELEMENT NUMBER
61102F

6. AUTHOR(S)
Anthony Guo Ningqun

5d. PROJECT NUMBER

5e. TASK NUMBER

5f. WORK UNIT NUMBER

7. PERFORMING ORGANIZATION NAME(S) AND ADDRESS(ES)
MONASH UNIVERSITY
WELLINGTON RD
CLAYTON, 3800 AU

8. PERFORMING ORGANIZATION REPORT NUMBER

9. SPONSORING/MONITORING AGENCY NAME(S) AND ADDRESS(ES)
AOARD
UNIT 45002
APO AP 96338-5002

10. SPONSOR/MONITOR'S ACRONYM(S)
AFRL/AFOSR IOA

11. SPONSOR/MONITOR'S REPORT NUMBER(S)
AFRL-AFOSR-JP-TR-2019-0028

12. DISTRIBUTION/AVAILABILITY STATEMENT
A DISTRIBUTION UNLIMITED: PB Public Release

13. SUPPLEMENTARY NOTES

14. ABSTRACT
The study shows that the range accuracy is proportional to the target reectivity but it decreases when the angle of incidence increases adheres to the bidirectional reection distribution function (BRDF). The presented ndings establish a better understanding of the inuence of target reection. Based on the operating principle of time slicing technique, fundamental of radiant energy, LADAR, and BRDF, theoretical derivation of the range gated reconstruction model is presented. The derived model shows the relationship and dependency of various parameters with respect to the reected laser intensity, SNR, and range accuracy. Accordingly, the algorithm of range estimation is improved by considering the energy attenuation and intensity variation due to distance and target reection, and range distortion because of the inhomogeneous illumination. From the experimental results, the proposed range estimation model shows a noticeable improvement as compared to the conventional weighted average model, which proves the validity of the formulation presented. By comparing the results to the accuracy estimated from the set-up specication, the proposed model is able to achieve comparable performance. A novel method is proposed detect underwater turbulence using a gated wavefront sensing system. The proposed method incorporated wavefront sensing and the range gated approach for effective underwater turbulence detection. Based on the operating principle of this technique, the laser emission and camera gating are simultaneously controlled to only capture the reflection from a known distance. The turbulence condition can be detected from the resulting wavefront reconstruction accordingly.
One Journal papers with two more journal paper on the way and one conference paper.

15. SUBJECT TERMS
Bi-directional Reflectance, Time-of-Flight principle, target reflection, Laser Detection And Ranging

Standard Form 298 (Rev. 8/98)
Prescribed by ANSI Std. Z39.18

DISTRIBUTION A: Distribution approved for public release.

16. SECURITY CLASSIFICATION OF:			17. LIMITATION OF ABSTRACT	18. NUMBER OF PAGES	19a. NAME OF RESPONSIBLE PERSON KIM, TONY
a. REPORT	b. ABSTRACT	c. THIS PAGE			
Unclassified	Unclassified	Unclassified	SAR		19b. TELEPHONE NUMBER *(Include area code)* 315-227-7008

Standard Form 298 (Rev. 8/98)
Prescribed by ANSI Std. Z39.18

DISTRIBUTION A: Distribution approved for public release.

Final Report

Investigate Target Reflection and Illumination Sensitivity in Range Gated Detection

Anthony Guo[1], Xin Wang[1], Chew Kuew Wai[2], Ching Seong Tan[3], Shoou-Jinn Chang[4]

1 Monash University Malaysia

2 University Tunku Abdul Rahman, Malaysia

3 Multimedia University, Malaysia

4 National Cheng Kung University, Taiwan

AOARD PROJECT FA2386-16-1-4115

Abstract

This project is a joint research project among the research teams from four institutions (Monash University Malaysia, University Tunku Abdul Rahman, Multimedia University and National Cheng Kung University), where the main objective is to investigate the effects induced by target reflection and illumination factors. Their impacts to the system performance are evaluated theoretically and experimentally.

The effect of target reflection was investigated from the perspectives of target reflectivity and angle of laser incidence. The study shows that the range accuracy is proportional to the target reflectivity but it decreases when the angle of incidence increases adheres to the bidirectional reflection distribution function (BRDF). Furthermore, ranging performance is also affected by the distortion caused by laser illumination and optical components. The distortion effect is radially symmetric and increases with the pixel’s distance from the image centre. These findings are integrated to propose a novel range estimation model. The proposed model outperforms the conventional weighted average model, which addresses the effects caused by the aforementioned factors to accomplish accurate reconstruction.

Furthermore, we propose a novel underwater turbulence detection method based on a gated wavefront sensing technique. The proposed method incorporated wavefront sensing and the range gated approach for effective underwater turbulence detection. Our experimental results prove that the proposed method can detect underwater turbulence conditions at different distances, and for different levels of turbulence. Due to the effectiveness of the proposed method, it has good potential, which will significantly benefit applications in underwater imaging, laser communication, oceanic exploration, etc.

1 Introduction

Laser sensing is highly advantageous for machine vision and reverse engineering due to its noncontact and non-destructive nature. Over the past decades, continuous growth is observed in laser ranging and its applications can be found in almost every sphere of life such as surveillance, military, oceanic and environmental research, miscellaneous industrial and day-to-day applications [1]. In a laser sensing system, laser shot interacts with the target surface to generate a backscatter signal to be received by the sensor which serves as the key information for range reconstruction. For the concern of direct range detection applied by Time-of-flight (TOF) and 3D imaging systems, amplitude and irradiance fluctuations are crucial [2]. Essentially, intensity of the detected laser pulse is a function of numerous parameters affected by few main components: laser source, sensor, target and atmospheric effect [3, 4]. These factors diminish the emitted power and could change the characteristics of the reflected laser signal. Therefore, it is necessary to analyse a range gated system from the perspective of the aforementioned parameters which help to improve the range accuracy.

The growing interest of adopting laser sensing approach in applications such as 3D vision, object modelling, target detection, and recovery [5, 6] inspires the study into the characteristic and influence of target reflection. [7] evaluated the effects of target shape and reflection characteristics, and demonstrated its importance to determine the shape and magnitude of the laser radar return. Study done by [8] showed differences in probability distribution of detected photons under background light and when target presents with specular and diffuse reflectivity. On the other hand, [9] claimed that the specular highlights and diffuse darkness in the target scene cause degradation in area based correlation, and thus proposed optimisation to handle high dynamic range surfaces. The characteristics of detection and ranging for objects of different dimensions were discussed in [10] which could be a valuable reference for object identification.

Specification of a laser as the illumination source is important and is defined by parameters such as wavelength, output power, pulse shape and width, repetition rate, beam divergence, etc. Diffraction effects of laser propagation through atmosphere and optical system are among the limiting factors to the system performance [11]. Radial distortion is a deficiency in straight lines transmission which has direct effect on the image geometry. Due to the radial distortion, a plane positioned parallel to the image plane is detected as a hyperbolic object. The parabolic depth needs to be transformed to the depth perpendicular to the image plane as correction [12]. Model-free approach without adopting a specific radial distortion model was used by [13].

2 Experimental setup

In order to investigate the effects induced by various influence factors, an experimental setup as illustrated in Figure 1 is used. A pulsed diode pumped solid state Q-switched Nd: YAG laser that operates at wavelength 532 nm with output energy up to 1mJ is used. Silicon high speed biased non-amplified photodetector with active diameter of 400 um and <300 ps rise/fall time is used to detect the laser pulses in the emitting or reflecting direction. Photodetector transforms the optical pulse into usable signal for analysis via oscilloscope.

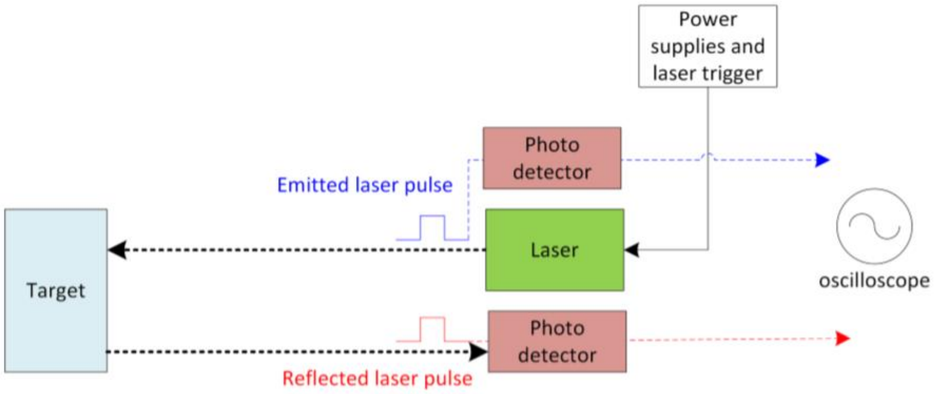

Figure 1 Schematic diagram of experimental setup

A backscatter signal is produced after the emitted laser pulse interacts with the target surface and is received by the detector in the form of time function. Two-way travel time across the distance between target and the detector is determined from the time difference between the emitted and reflected laser pulse. Correspondingly, the distance or range r can be obtained based on the Time-of-fight principle.

3 Investigation of the influence of target reflection

From Laser Detection And Ranging (LADAR) range equation, the detected signal P_r is defined as [14]:

$$P_r = \frac{\eta_{sys}\eta_{atm} D^2 \rho A P_t}{r^2 \theta_R (\theta_t r)^2} \qquad (1)$$

P_r and P_t are the received and transmitted signal across range r, η_{sys} and η_{atm} represent the system efficiency factor and atmospheric transmission loss caused by absorption and scattering. D is the diameter of receiver aperture and ρ is the target surface reflectivity. θ_t represents the laser transmitter beam diameter and angular divergence and θ_R is the solid angle over which radiation is dispersed upon reflection.

Assume the target surface area A is equal to the projected area of laser beam [14]:

$$A = \frac{\pi \theta_t^2 r^2}{4} \qquad (2)$$

Eq. (1) can be simplified as:

$$P_r = \frac{\pi \eta_{sys}\eta_{atm} D^2}{4r^2} \frac{\rho}{\theta_R} P_t \qquad (3)$$

$\frac{\rho}{\theta_R}$ corresponds to the target reflection characteristics which we can represent with a Bidirectional Reflection Distribution Function (BRDF) model [15] where K_S and K_D are the specular and diffuse reflection constants, θ is the angle of incidence and reflection, s is the surface slope, and m is the diffusivity coefficient.

$$BRDF = \frac{K_S}{\cos^6\theta}\exp\left(\frac{-\tan^2\theta}{s^2}\right) + K_D\cos^m\theta \quad (4)$$

Gaussian form is commonly assumed for temporal function of the transmitted laser pulse $P_t(t)$ where P_o represents the transmitted power and σ_p denotes the standard deviation of laser pulse [16]:

$$P_t(t) = \frac{P_o}{\sqrt{2\pi}\sigma_p}\exp\left(\frac{-t^2}{2\sigma_p^2}\right) \quad (5)$$

Accordingly, Eq. (3) can be written as:

$$P_r(t) = \frac{\pi\eta_{sys}\eta_{atm}D^2}{4r^2}\left[\frac{K_S}{\cos^6\theta}exp\left(\frac{-tan^2\theta}{s^2}\right) + K_D cos^m\theta\right]\frac{P_o}{\sqrt{2\pi}\sigma_p}exp\left(\frac{-t^2}{2\sigma_p^2}\right) \quad (6)$$

Reflected intensity strongly depends on the characteristics of the target surface [17]. Although Lambertian target (ideal diffuse surface) is commonly assumed due to its simplicity, target reflection is in fact far more complicated and BRDF concept is normally used to describe that. Our theoretical model has adopted a BRDF model which consists of specular and diffuse reflection to analyze the characteristics of reflected intensity in this study. Reflection off a rough surface returned in many directions leads to diffuse reflection while reflection from a smooth surface remains concentrated with the angle of reflection which causes specular reflection. Any target surface practically exhibits mixture of specular and diffuse behavior per surface properties such as roughness and absorption level.

Simulation based on the BRDF model is shown in Figure 2. Four examples of target surface model are compared. These include two extreme cases of pure specular and pure diffuse surface models, and two examples of mixed components surface with different ratio of surface glint to diffuse behaviour given by specular and diffuse reflection constants i.e. K_S/K_D. The amplitude of the reflection is maximum when angle of incidence θ=0 degree and decreases when θ increases, adheres to the BRDF model. As a result, the decreased intensity causes the reduced SNR which gives rise to range error.

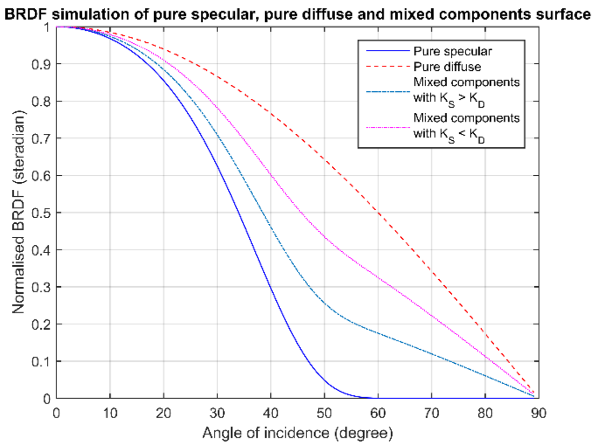

Figure 2 BRDF simulation as a comparison of different target surface models

For our experimental study, various target surface materials and roughness are tested. Figure 3 compares the range error for target surfaces captured at 5 m and the results are analyzed based on average of 30 measurements. From the results, we observe that the range error is higher for rough and weak reflective surfaces as compared to smooth and strong reflective surfaces where these surfaces can be modelled using BRDF described in our theoretical model. In addition, the effect of angle variation is evaluated for various target surfaces where the corresponding range errors from total of 30 measurements are shown in Figure 4. It can be clearly seen that the range error is minimum at zero angle of incidence θ=0 degree and increases with the angle of incidence in general. This has demonstrated the angular dependency which agrees with the theoretical model discussed.

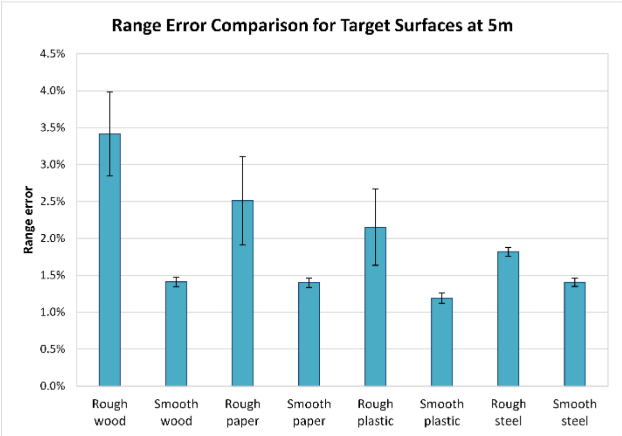

Figure 3 Comparison of range error for target surfaces with different reflectivity and roughness

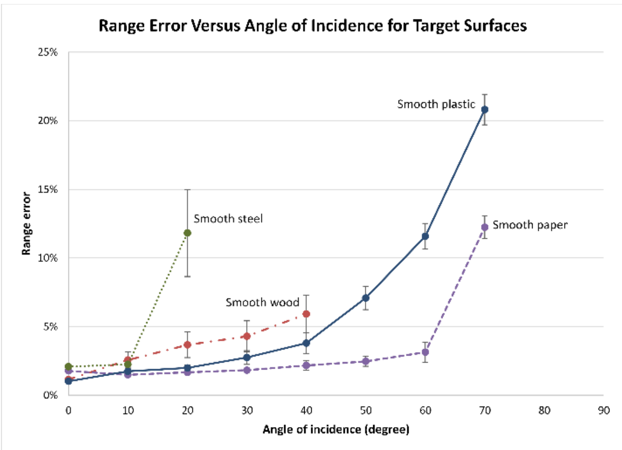

Figure 4 Comparison of range error versus angle of incidence for target surfaces with different reflectivity

4 Investigation of the influence of laser illumination

In a laser scanning system, the laser illumination is diverged to cover the entire target scene as illustrated in Figure 5. The centre of illumination is assumed at the image centre and covers an area within (x_{max},y_{max})with half diverging cone propagation of angle φ. x and y represent the horizontal and vertical position of an image pixel with diverging angle θ.

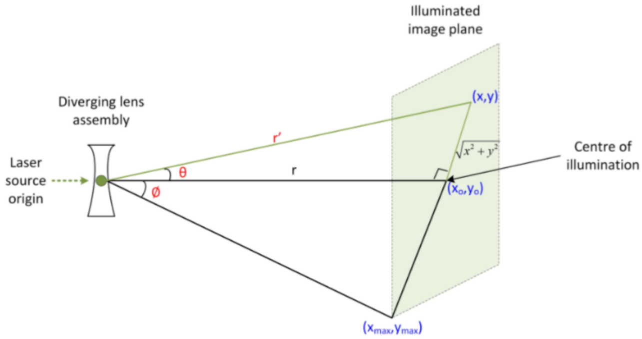

Figure 5 Laser illumination is diverged to cover the target scene in a laser scanning system

Based on the needs of the application, the diverging angle spreads the laser beam ranging from a few mille-radians to radian to vary the field of illumination accordingly. Laser illumination with diverging lens assembly results in additional effects on the illuminated scene, reflection from the target, and image generation which should be considered. Deficiency in straight lines transmission results in radial distortion which has direct effect on the reflection and image geometry.

Figure 5 shows the difference between orthogonal distance r and radial distance r′, which leads to the range distortion. Radial distance r′ is expressed as:

$$r' = \sqrt{x^2 + y^2 + r^2} \quad (7)$$

Radial distance r' is often approximated as orthogonal distance r with the following assumptions where x and y indicate the position of the image pixel from the centre of illumination.

$$r' = r \quad if \quad x = 0, y = 0 \quad or \quad r \gg x, y \quad (8)$$

Orthogonal distance r is normally used with assumption that the illumination is at the centre or perpendicular to the image plane. However, this ideal condition is only true around the centre of illumination where the laser approximates to directional lighting [18]. Most likely pixels within the angular space receive maximum reflection where θ=0 while other pixels exhibit variation due to the illuminate direction [19, 20]. Intensity decreases as the pixels distance from the centre of illumination as illustrated in Figure 6 and higher pixel values are observed towards the centre of the image. This inhomogeneous illumination results in radial distortion which affects the image geometry and range information.

In general, radial distortion can be expressed as follows [21]:

$$r^d = e + \lambda(r^u - e) \quad (9)$$

where r^d and r^u are the distorted and undistorted points, respectively. e denotes the centre of distortion and λ represents the distortion ratio. In our context, we assume the centre of distortion equals to the centre of illumination which is the image centre.

Distortion ratio is equal to unity near the image centre to give r=r'. Accordingly, we can model the radial distortion as follows, where r is considered as the distorted point r^d and r' as the undistorted points

$$r = \lambda(r') \quad (10)$$

The distortion effect can be regarded as radially symmetry because the lenses aretypically ground to be circularly symmetric. This means that the distortion ratio λ is a function of the image pixel position or radius. In this case, we can model the distortion ratio λ as a function of the angular difference between r′ and r, which is bounded by the maximum diverging angle φ. Two assumptions are made on the range distortion. Firstly, the distortion ratio is unity at the centre of illumination i.e. r′=r and the distortion effect increases (λ decreases<1) as the image pixels(x, y) move radially from the centre. λ can be modelled to decrease with respect to the angular difference θ(x, y) between r and r′ where $0<\lambda\leq 1$.

$$\lambda = \frac{r}{r'} = cos\theta(x,y) \quad (11)$$

Secondly, the distortion is radially symmetry within the illuminated area (x_{max}, y_{max}). Θ depends on the position of the image pixel(x, y) and the maximum diverging angle φ, which is expressed as:

$$\theta(x,y) = (\frac{\sqrt{x^2+y^2}}{\sqrt{x_{max}^2+y_{max}^2}})\phi \quad (12)$$

Accordingly, we propose distortion estimation based on the divergence angle of illumination φ and the position of image pixel(x, y) relative to the centre of illumination (0,0) where the distortion ratio λ is formulated as:

$$\lambda = cos\theta(x,y) = cos[(\frac{\sqrt{x^2+y^2}}{\sqrt{x_{max}^2+y_{max}^2}})\phi] \quad (13)$$

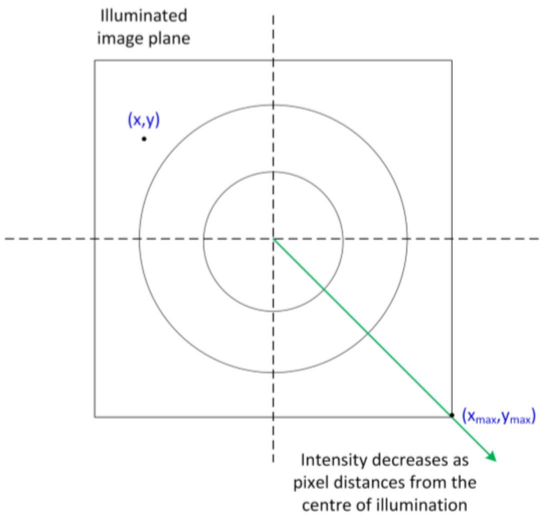

Figure 6 Illustration of an illuminated image plane where intensity decreases as pixel distances from the image centre

We evaluated the distortion effect experimentally. Laser is emitted towards the target surface with different angles of incidence to produce a back scatter signal, which is received by photodetector to determine the range. Analysis of the experimental data from reflected laser measurements is shown in Figure 7. As the angle of laser incidence increases, the resulted range calculated from weighted average model shows higher error i.e. greater distortion. This can be related to the increase of angular difference between *r* and *r′* when image pixels are located away from the centre of illumination.

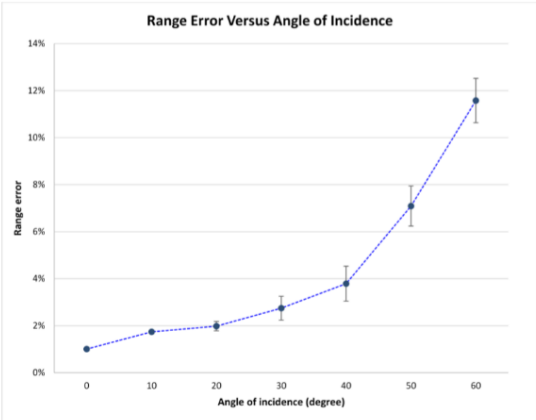

Figure 7 Range deviates as the angle of laser incidence θ increases based on the reflected laser measurements

5. Proposed range estimation model

A new range estimation model is proposed to alleviate the effects induced by the influence factors studied in this project.

5.1 Range estimation model

In a range gated system with time slicing reconstruction, SNR is expressed in term of the reflected laser intensity I_i and associated noises δI_i from a sequence of image slices $I_i(x,y)$.

$$SNR = \frac{\sum_i I_i}{\sqrt{\sum_i (\delta I_i)^2}} \quad (14)$$

By considering random noise where $(\delta I_i)^2 \approx I^i$, SNR can be simplified as:

$$SNR \approx \frac{\sum_i I_i}{\sqrt{\sum_i I_i}} = \sqrt{\sum_i I_i} \quad (15)$$

Theoretically, *SNR* can be estimated from the system parameters as follows:

$$SNR \approx \sqrt{\sum_i I_i} = \sqrt{\frac{\sigma}{t_{step}} max(I_i)} \quad (16)$$

where the total intensity in an image pixel $I=\sum_i I_i$ is contributed by number of time slices, which is given by σ/t_{step} factor. Variance of the measured travel time σ^2 depends on the laser pulse width and camera gate time while t_{step} is the delay time step used for images acquisition. Accordingly, range accuracy is estimated as [22]:

$$\delta r \approx \frac{1}{2}\frac{c\sigma}{SNR} \quad (17)$$

As can be seen, range accuracy is governed by two parameters: σ and *SNR*. In general, σ is affected by the system specification, i.e. laser and camera, where the range accuracy can be improved by the hardware advancement. On the other hand, *SNR* is proportional to the reflected laser intensity which can be influenced by other condition such as target reflection.

Besides the system specification, range accuracy also relies on *SNR* which can be affected by various factors. For example, *SNR* drops approximately r−1 across distance r due to the decreased reflected laser intensity. When the distance increases by 10 times, *SNR* decreases accordingly. In another words, we may improve the range algorithm to achieve comparable performance without having to upgrade the system which involves additional cost.

Theoretically, the system performance can be optimised if the effect of influence factors can be fully compensated in the range algorithm. Therefore, we propose a new range estimation model based on LADAR equation and BRDF model.

Reflected laser intensity captured in an image pixel Ii is the incident energy of laser pulse P_r integrated when the camera gate $G(t)$ opens, which is expressed as:

$$I_i = \int P_r(t - \frac{2r}{c})G(t - t_i)dt. \quad (18)$$

Based on time slicing technique, we obtain $I(x,y)$ as:

$$I(x,y) = \frac{\int P_r(x,y,t)dt \int G(\tau)d\tau}{t_{step}} \quad (19)$$

By substituting $P_r(x,y,t)$ (Eq.6) and assuming $G(\tau) = 1$ when $0 \leq \tau \leq$ tgate, $I(x,y)$ is expressed as:

$$I(x,y) = \frac{\pi\eta_{sys}\eta_{atm}D^2}{4r^2 t_{step}}[\frac{K_S}{cos^6\theta}exp(\frac{-tan^2\theta}{s^2}) + K_D cos^m\theta]\frac{P_o}{\sqrt{2\pi}\sigma_p}\int_{-\infty}^{\infty} exp(\frac{-t^2}{2\sigma_p^2})dt \int_0^{t_{gate}} d\tau \quad (20)$$

We further simplify $I(x,y)$ into:

$$I(x,y) = \frac{\pi\eta_{sys}\eta_{atm}D^2}{4r^2}[\frac{K_S}{cos^6\theta}exp(\frac{-tan^2\theta}{s^2}) + K_D cos^m\theta]P_o\frac{t_{gate}}{t_{step}} \quad (21)$$

A pixel intensity $I(x, y)$ is influenced by multiple factors including laser, detector, target, and atmospheric parameters. Based on time slicing technique, the camera gate t_{gate} and time step t_{step} are fixed during range gated images acquisition. The system performance is therefore affected by the intensity variation factors as follows:

$$\Delta I(x,y) = \frac{\pi\eta_{sys}\eta_{atm}D^2}{4r^2}\left[\frac{K_S}{cos^6\theta}exp\left(\frac{-tan^2\theta}{s^2}\right) + K_D cos^m\theta\right] \quad (22)$$

Under the same setup condition, system efficiency η_{sys}, atmospheric transmission loss factor η_{atm} caused by absorption and scattering, and receiver aperture's diameter D can be regarded as constants. Depending on the target surface properties and BRDF reflection characteristics, K_S and K_D are the specular and diffuse reflection constants where K_S K_D indicates the ratio of surface glint to diffuse behaviour. θ is the angle of incidence and reflection, *s* is the surface slope, and m is the diffusivity coefficient. By considering the four factors we study so far: distance, target reflection BRDF, range distortion, and noise influences, the findings can be incorporated to propose a range reconstruction model for better 3D solution. The average two-way travel time based on the received pixel intensity over time slices can be obtained as:

$$< t > (x,y) = \frac{1}{\cos\left[\left(\frac{\sqrt{x^2+y^2}}{\sqrt{x_{max}^2+y_{max}^2}}\right)^k \phi\right]} \frac{\sum_{i=1}^{n}\left[\frac{K_S}{cos^6\theta}exp\left(\frac{-tan^2\theta}{s^2}\right) + K_D cos^m\theta\right]^{-1} w_i I_i(x,y) t_i^3}{\sum_{i=1}^{n}\left[\frac{K_S}{cos^6\theta}exp\left(\frac{-tan^2\theta}{s^2}\right) + K_D cos^m\theta\right]^{-1} w_i I_i(x,y) t_i^2} \quad (23)$$

Accordingly, the average range r can be determined as:

$$\begin{aligned} < r > (x,y) &= \frac{c}{2\cos\left[\left(\frac{\sqrt{x^2+y^2}}{\sqrt{x_{max}^2+y_{max}^2}}\right)^k \phi\right]} \frac{\sum_{i=1}^{n}\left[\frac{K_S}{cos^6\theta}exp\left(\frac{-tan^2\theta}{s^2}\right) + K_D cos^m\theta\right]^{-1} w_i I_i(x,y) t_i^3}{\sum_{i=1}^{n}\left[\frac{K_S}{cos^6\theta}exp\left(\frac{-tan^2\theta}{s^2}\right) + K_D cos^m\theta\right]^{-1} w_i I_i(x,y) t_i^2} \\ &= \frac{1}{\cos\left[\left(\frac{\sqrt{x^2+y^2}}{\sqrt{x_{max}^2+y_{max}^2}}\right)^k \phi\right]} \frac{\sum_{i=1}^{n}\left[\frac{K_S}{cos^6\theta}exp\left(\frac{-tan^2\theta}{s^2}\right) + K_D cos^m\theta\right]^{-1} w_i I_i(x,y) r_i^3}{\sum_{i=1}^{n}\left[\frac{K_S}{cos^6\theta}exp\left(\frac{-tan^2\theta}{s^2}\right) + K_D cos^m\theta\right]^{-1} w_i I_i(x,y) r_i^2} \end{aligned} \quad (24)$$

5.2 Model validation and results analysis

Two objects are tested where Object 1 has higher reflectivity relative to Object 2. Figure 8 shows the raw gray-scale image of the test objects acquired using the range gated imaging system.

(a) Object 1 (b) Object 2

Figure 8 Raw image of the test objects captured by the range gated imaging system

Object 1 and Object 2 have 0.48m and 0.4m depth measured from background respectively. The experimental setup used and the resulted range accuracy δr ≈8.894mm in the ideal scenario. The corresponding % depth error can be calculated as

$$\% \text{ depth error} = \frac{\delta r}{\text{object depth}} * 100 \quad (25)$$

With the system range accuracy δr≈8.894mm, it is estimated to give depth error ≈1.85% and 2.22% for Object 1 and Object 2.

The proposed range estimation model is used to determine the object's depth from the 2D images sequence of the target scene and the calculated result is compared to the weighted average model in Table 1. As the test objects have homogeneous surface material, target reflection BRDF compensation is not considered because the reflectivity is assumed to be uniform. Based on the conventional weighted average method, depth error of 12.65% and 14.11% are observed for Object 1 and Object 2. The proposed range estimation model reduces the depth error to 2.26% and 2.93% for Object 1 and Object 2 respectively. Figure 9 shows the graphical representation of the 3D surface reconstruction using the proposed range estimation model for Object 1 and Object 2 respectively.

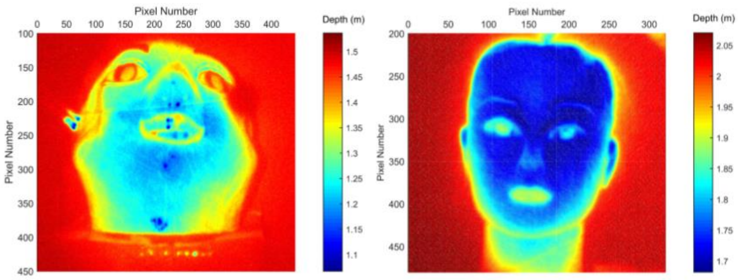

(a) Object 1 (b) Object 2

Figure 9 3D surface reconstruction of the test objects using the proposed range estimation model

Table 1 Absolute depth error (%) calculated based on the conventional weighted average and the proposed range estimation model as compared to the estimated depth error per setup specification in ideal scenario

Test object	Depth error per setup specification	Weighted average model	Proposed range estimation model
Object 1	1.85%	12.65%	2.26%
Object 2	2.22%	14.11%	2.93%

From Table 1,it can be seen that the proposed range estimation model perform better, results in smaller depth error as compared to the conventional weighted average model which is commonly used. Based on the system specification used, the range accuracy in ideal scenario is estimated as≈1.85% and 2.22% for Object 1 and Object 2 respectively. This range accuracy calculated from the experimental setup specification is a rough estimation and deviation of the depth error is expected. From the results presented, suffice to say, the proposed model outperforms the conventional weighted average model to give better range estimation for 3D range gated reconstruction.

6 Turbulence detection using gated wavefront sensing

Underwater detection is greatly affected by the turbulence effect, where the acquired image suffers excessive noise, blurring, and deformation. In this study, we combine wavefront sensing and the time-of-flight (TOF) range-gated principle to detect underwater turbulence.

6.1 Gated wavefront sensing system

We design a gated wavefront sensing system to detect the turbulence effect underwater, as illustrated in Figure 10. The system components are a pulsed laser, beam-splitting (BS) prisms, a collimator, a photodetector, the wavefront sensing assembly (e.g.,lenslet and gated intensified CCD camera), and delay generator for system triggering and synchronization.

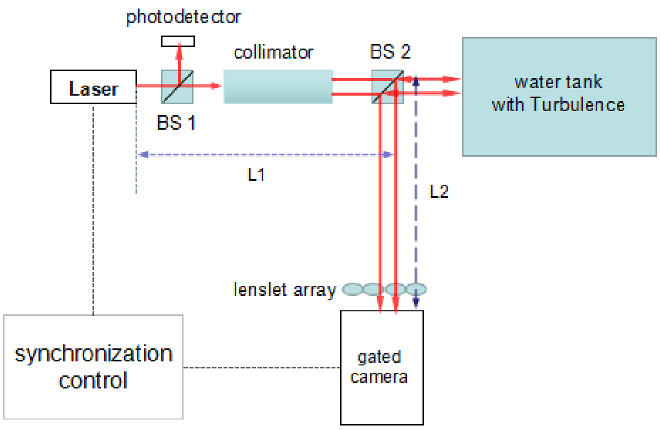

Figure 10 Schematic diagram of the gated wavefront sensing system.

Light passes through a series of components that are separated by a distance along the light path, r. This can be expressed as follows according to the TOF principle:

$$r = \frac{vt_0}{2} \qquad (26)$$

where t_0 is the travel time of the laser pulse, and $r$is the speed of light in the working condition. In our setup, we set the distance from the laser to the second prism, BS2, as equal to the distance from the BS2 prism to the range-gated camera (L1=L2), as shown in Figure 10, in order to simplify the calculation. The front part of each laser pulse will carry the wavefront information of the underwater turbulence from different distances.

A range-gating process starts when the laser emits a pulse. The camera gate is kept closed at all times, and is only opened for a short time when the laser pulse returns to the camera after hitting the target. Thus, only light that arrives at the sensor within the right timing window can contribute to the imaging process. After synchronization, the gated wavefront sensor samples the incident wavefront from different interfaces by means of a lenslet array. The wavefront is spatially sampled and focused by the lenslet array on the camera.

6.2 Wavefront Reconstruction

In our gated wavefront sensing system, a lenslet array is used to focus the incoming wavefront onto a range-gated camera. This microlenslet array partitions the reflected wavfront into a larger number of smaller wavefronts, each of which is focused on a small spot on the sensor. The spatial displacement of each spot is a direct measure of the local slope of the incident wavefront as it passes through the lenslet. The integration of these slope measurements can reconstruct the shape of the wavefront.

The centroid locations of the focal points are then compared with the reference focal points. The displacement of each centroid location reflects the wavefront slope. The wavefront information obtained at a water velocity of 0L/min is used as the reference wavefront. The schematic diagram of the wavefront sensor is shown in Figure 11.

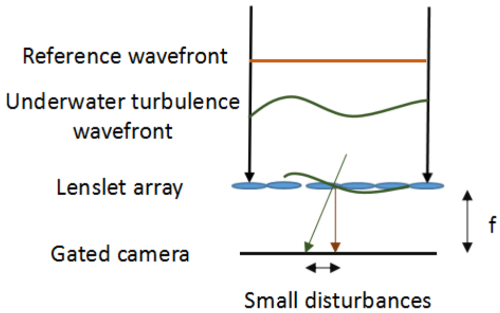

Figure 11 Schematic diagram of the wavefront sensor.

Small disturbances, $\frac{\partial W(x,y)}{\partial x}$ and $\frac{\partial W(x,y)}{\partial y}$, are introduced to the sampling aperture. The centroid displacements reflect the wavefront slope change, $\frac{\partial W(x,y)}{\partial x}$ and $\frac{\partial W(x,y)}{\partial y}$, which are defined as:

$$\frac{\partial W(x,y)}{\partial x} = \frac{\Delta x}{f}, \quad \frac{\partial W(x,y)}{\partial y} = \frac{\Delta y}{f} \qquad (27)$$

where Δd_x is the average slope over a subaperture diameter in the x direction; Δd_y is the average slope over a subaperture diameter in the *y* direction; Δx is the measured spot centroid displacement from the reference in the x direction; and f is the focal length of the lenslet array.

The center of each spot can be calculated as follows:

$$X_c = \frac{\sum_{i,j}^{L,M} x_i I_{ij}^{\alpha}}{\sum_{i,j}^{L,M} I_{ij}^{\alpha}} \qquad (28)$$

$$Y_c = \frac{\sum_{i,j}^{L,M} y_j I_{ij}^{\alpha}}{\sum_{i,j}^{L,M} I_{ij}^{\alpha}} \qquad (29)$$

where X_c and Y_c are the centroid position of the spot; I_{ij}^{α} is the α th high intensity value in this spot sub-area; x_i and y_j are the coordinates of the pixel in the whole spot image; and L and M are the numbers of the pixels along x and y directions in the window, respectively.

The slope matrix, or curvature matrix, is obtained for further reconstruction using an iterative method in orderto generate the surface. In this study, we use the Zernike polynomials. A distorted wavefront $W(x, y)$ is represented by a Zernike polynomial as:

$$W(x,y) = \sum_{i=0}^{k} C_k Z_k(x,y) \qquad (30)$$

The reconstructed wavefront is then calculated using Eq. (30). The deconvolution of blurred images can then be done using the wavefront obtained. The acquired image, v, and its correlation with the original image, u, can be described as:

$$v = H(u) + p \qquad (31)$$

where p is the noise from image acquisition and the inaccuracies in wavefront reconstruction, and H denotes the convolution operator resulting from the reconstructed wavefront. The deconvolution of the acquired image would then be a minimization function [23]. In order to obtain the original image, u, the following equation is used:

$$u' = \min_u \left\{ \frac{1}{2} \|H(u) - p\|_2^2 + \Delta \|u\| \right\} \qquad (32)$$

with Δ being the regularization parameter.

6.3 Experimental results and discussion

Experiments were carried out in a long water tank. The turbulence level was simulated by controlling the flow rate of the water. Other environmental factors, such as the temperature of the water, were kept constant, as we only considered the effects of spatial turbulence due to the flow of water. Actually, water disturbance, density, temperature, and other non-uniform factors will cause a random change in the refractive index of macromolecules in water. Underwater turbulence causes small changes of the refractive index ($\Delta n \approx 10^{-6}$), which caused a very small angular scatter of the beam. In general, the bidirectional reflectance distribution function (BRDF) is an accurate description of the surface of the light reflection of the basic parameters. However, the underwater environment cannot be expressed by a simple negative exponential decay function. So, it is more difficult to measure its intensity distribution by conventional methods. The reflection ratio of light intensity in an underwater situation is about 20–30%. Therefore, we use a 532-nm laser and a time-gated camera to reduce the impact of underwater reflectance, and get the focal imaging.

In our synchronization control system, water flows into the tank at a distance of four meters from the wavefront sensing system. The flow rate can be controlled to create a turbulence condition. Figure 12 shows the gated wavefront sensing system and the water tank control system.

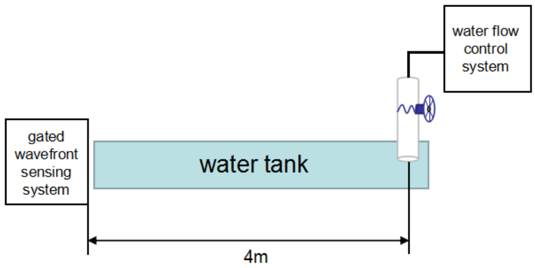

Figure 12 Gated wavefront sensing system and water tank control system

Regarding the sensitivity and the dynamic range of the sensor, the gated wavefront sensor is limited by the focal length and the pitch of the microlens array, as well as the pixel size of the camera used. The microlens array we used in our setup has a focal length of 6.7mm and a pitch of 150μm, and the ICCD camera has a pixel size of 17.8μm. Therefore, the corresponding sensitivity$\left(\theta_{\min}\right)$ and dynamic range$\left(\theta_{\max}\right)$ can be calculated accordingly. The calculation equations are as follows:

$$\theta_{\min} = \frac{P}{f} = \frac{17.8\times10^{-3}}{6.7} = 0.002657\text{rad} = 0.1522^{\circ} \qquad (33)$$

$$\theta_{\max} = \frac{D}{2f} = \frac{150\times10^{-3}}{2\times6.7} = 0.011194\text{rad} = 0.6414^{\circ} \qquad (34)$$

Subsequent experimental results show that the sensitivity and the dynamic range of the sensor can be effectively measured. We acquired the focal image with the flow rate of 0L/min as a reference for wavefront reconstruction. Four distances were selected for turbulence comparison, namely: 1m, 2m, 3m, and 4m. The water flow rate was set at 40L/min. Figure 13 shows the focal spot images from different distances in the water tank with turbulence.

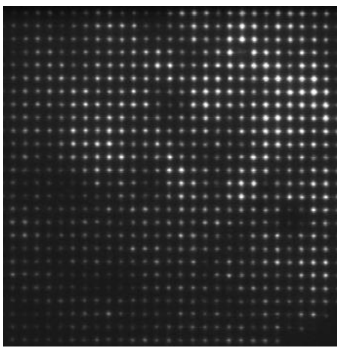

(a)

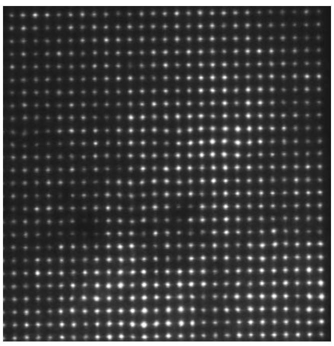

(b)

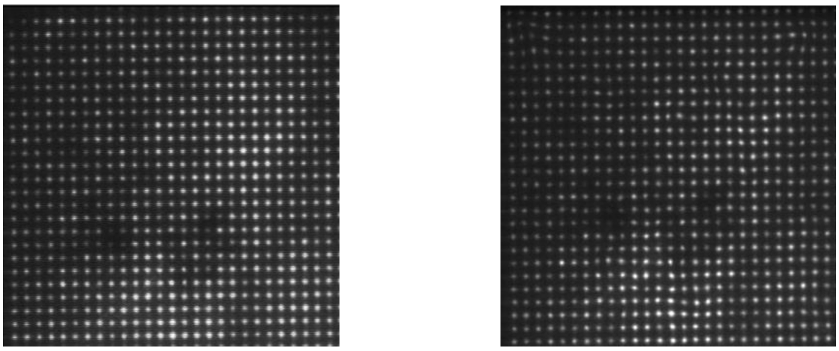

(**c**) (**d**)

Figure 13 Focal spot images acquired from different distances. (a) Focal spot image from 1m; (b) focal spot image from 2m; (c) focal spot image from 3m; (d) focal spot image from 4m.

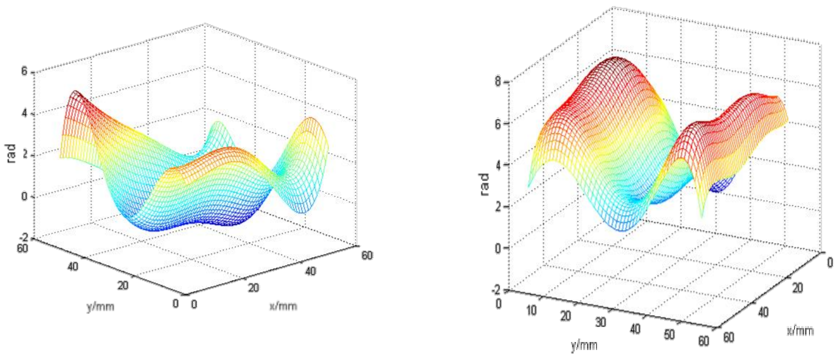

(**a**) (**b**)

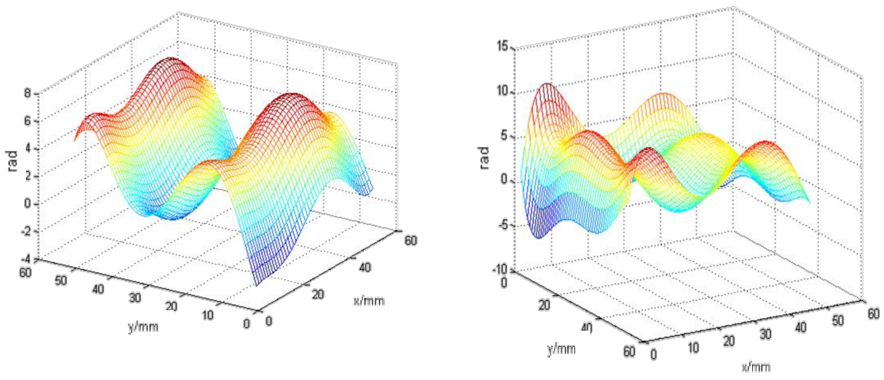

(**c**) (**d**)

Figure 14 The results of wavefront reconstruction at different distances: (a) 1 m; (b) 2 m; (c) 3 m; and (d) 4 m.

In general, the existing detection methods are ineffective for detecting underwater turbulence, because of the scattering problem. As shown in Figure 14, we are able to detect turbulence changes at different distances using the proposed gated wavefront sensing. The reconstructed wavefronts were calculated in radians where the coefficients were multiplied by $2\pi/\lambda$. λ is the wavelength. The vertical axis is the phase in radians, and the *xy* plane, is the space where the phase is measured. At the distance of 4m from our sensing system (where turbulence originated from the water flow in), the wavefront reconstruction model is relatively volatile. At distances further away from the water inlet, the turbulence effect becomes weaker, and the reconstructed wavefront image gradually flattens out, as shown in Figure 14. This verified that the underwater turbulence can be detected by the proposed gated wavefront sensing system.

In our next set of experiments, we set the distance at 4m (where the flow rate can be controlled to create a turbulence condition) and varied the velocity of water flow. Figure 15 shows the focal spot images acquired from the same distance i.e., 4m, with different water flow rates. Figure 16 shows the wavefront reconstruction results for 10L/min, 20L/min, 30L/min, and 40L/min, respectively.

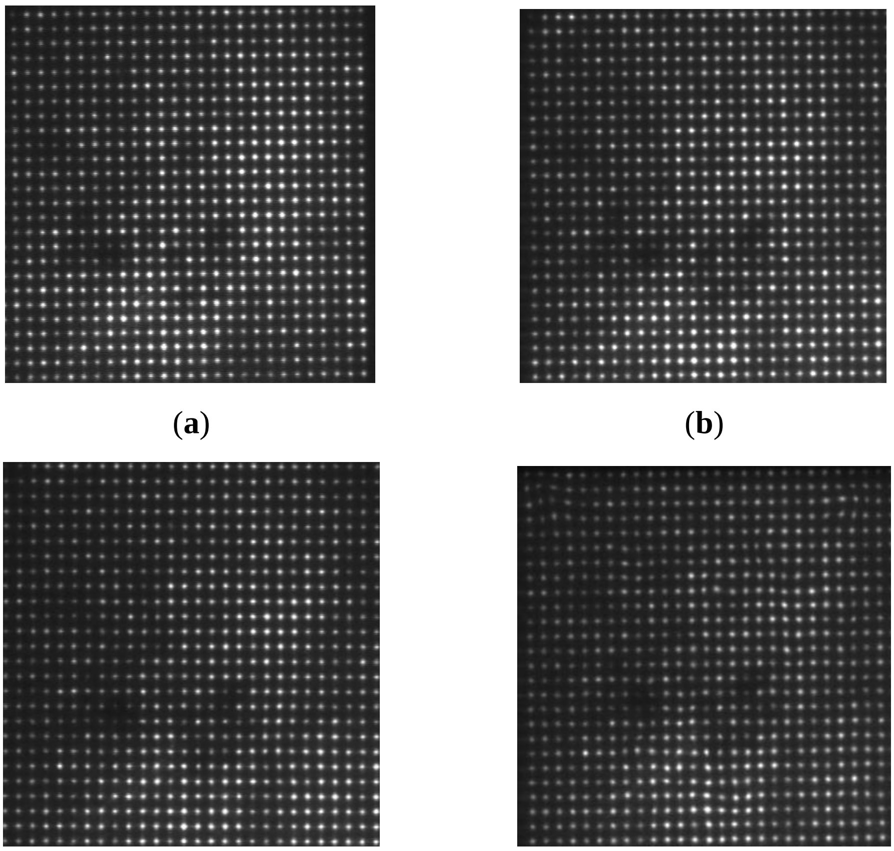

(**a**) (**b**) (**c**) (**d**)

Figure 15 Focal spot images acquired from the same distance i.e., 4m with different water flow rates: (a) 10L/min; (b) 20L/min; (c) 30L/min; (d) 40L/min.

Using the reference wavefront obtained from a flow rate of 0L/min, the wavefronts above in Figure 16 were obtained. As the turbulence generated is spontaneous and impromptu, repeated measurements would not yield similar wavefronts. Therefore, these wavefronts were characterized based on the relative difference between the above spot images and the reference 0L/min spot image. It can be seen that the peak-to-valley ratio of the reconstructed wavefronts relative to the reference wavefront increased as the flow rate increased. Therefore, there was indeed distortion in the wavefronts due to the induced turbulence from the turbulent flow of water at 4m.

As shown in Figure 16, our method is able to detect turbulence changes at different flow rates of water using the proposed gated wavefront sensing system. At the distance of 4m from our sensing system (where turbulence originated from the water flow in), the higher the water flow rates, the more volatile the wavefront reconstruction model will be. This proves the validity of the proposed gated wavefront sensing system for detecting underwater turbulence.

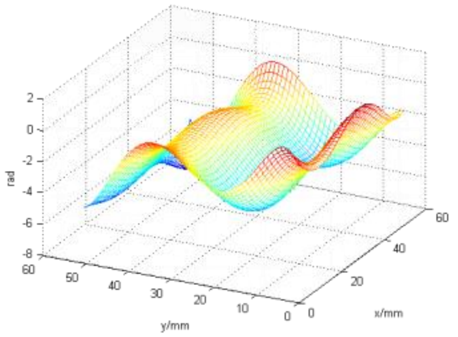

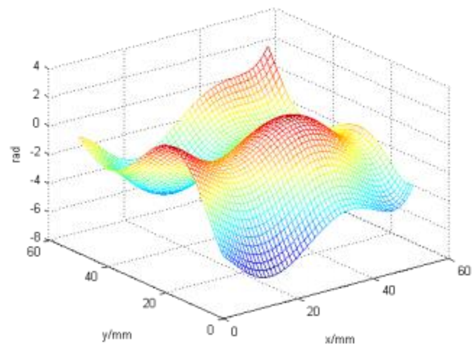

(**a**) (**b**)

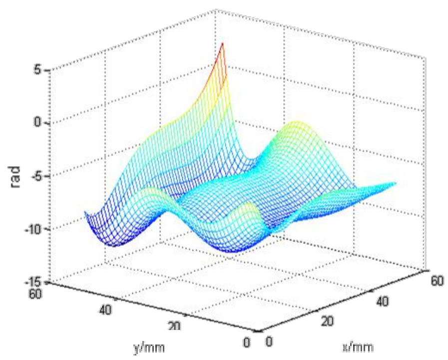

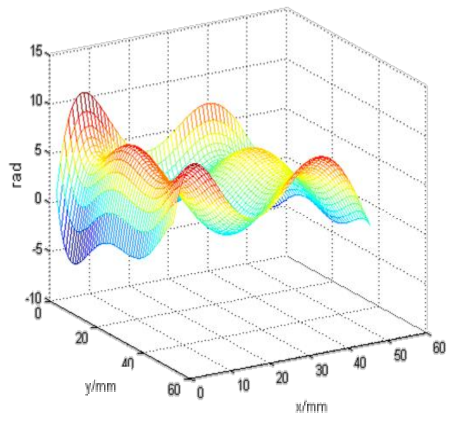

(**c**) (**d**)

Figure 16 The results of wavefront reconstruction at the same distance with different water flow rates: (a) 10L/min; (b) 20L/min; (c) 30L/min; and (d) 40L/min.

7 Conclusion

In summary, the achievement and impact of the project can be shown as follows:

1) The study shows that the range accuracy is proportional to the target reflectivity but it decreases when the angle of incidence increases adheres to the bidirectional reflection distribution function (BRDF). The presented findings establish a better understanding of the influence of target reflection.
2) Based on the operating principle of time slicing technique, fundamental of radiant energy, LADAR, and BRDF, theoretical derivation of the range gated reconstruction model is presented. The derived model shows the relationship and dependency of various parameters with respect to the reflected laser intensity, SNR, and range accuracy. Accordingly, the algorithm of range estimation is improved by considering the energy attenuation and intensity variation due to distance and target reflection, and range distortion because of the inhomogeneous illumination. From the experimental results, the proposed range estimation model shows a noticeable improvement as compared to the conventional weighted average model, which proves the validity of the formulation presented. By comparing the results to the accuracy estimated from the set-up specification, the proposed model is able to achieve comparable performance.
3) A novel method is proposed detect underwater turbulence using a gated wavefront sensing system. The proposed method incorporated wavefront sensing and the range gated approach for effective underwater turbulence detection. Based on the operating principle of this technique, the laser emission and camera gating are simultaneously controlled to only capture the reflection from a known distance. The turbulence condition can be detected from the resulting wavefront reconstruction accordingly.
4) The outcome of this research has generated 2 ISI Q 1 journal papers and 1 international conference paper. And 2 more journal papers are under review.

   Journal papers:
   Sing Yee Chua, Ningqun Guo, Ching Seong Tan, Xin Wang, Improved Range Estimation Model for Three-Dimensional (3D) Range Gated Reconstruction, Sensors, 17(9):2031, 2017.(ISI, Q1, IF: 2.475)

   Ying Bi, Xiping Xu, Sing Yee Chua, Eddy Mun Tik Chow, Xin Wang, Underwater Turbulence Detection Using Gated Wavefront Sensing Technique, Sesors, 18(3), 798, 2018. (ISI, Q1, IF: 2.475)

   Conference paper:
   Sing Yee Chua, Ningqun Guo, Ching Seong Tan, Kuew Wai Chew, Shoou-Jinn Chang, Xin Wang, System Setup Consideration for Range Gated Imaging, Conference on Lasers and Electro-Optics Pacific Rim (CLEO-PR) 2017, Singapore

5) The Postdoc under this project has successfully obtained Assistant Professor position. And 1 PhD student has been enrolled to conduct the research in this area.
6) This project been highlighted as featured research in "Monash Annual Review 2016".

References

[1] M.-C. Amann, T. Bosch, M. Lescure, R. Myllylä, and M. Rioux, "Laser ranging: a critical review of usual techniques for distance measurement", Opt. Eng., vol. 40, no. 1, p. 10, Jan. 2001.

[2] A. Kolb, E. Barth, R. Koch, and R. Larsen, "Time-of-Flight Sensors in Computer Graphics", 2009.

[3] C. Tan, G. Seet, A. Sluzek, D. He, "A novel application of range-gated underwater laser imaging system (ULIS) in near-target turbid medium", Opt. Lasers Eng., 43 (9), 995-1009, 2005.

[4] B. Höfle and N. Pfeifer, "Correction of laser scanning intensity data: Data and model-driven approaches", ISPRS J. Photogramm. Remote Sens., vol. 62, no. 6, pp. 415–433, Dec. 2007.

[5] A. Velten, T. Willwacher, O. Gupta, A. Veeraraghavan, M. G. Bawendi, R. Raskar, "Recovering three-dimensional shape around a corner using ultrafast time-of-flight imaging", Nature communications, Vol 3, 745, 2012.

[6] D. Lv, J.-F. Sun, Q. Li, and Q. Wang, "Model-based recognition of 3D articulated target using ladar range data", Appl. Opt., vol. 54, no. 17, p. 5382, 2015.

[7] E. Nava, E. Stucchi, "Development of lasers for spaceborne doppler wind lidar applications", Opt. Lasers Eng. 39 (2) 255-263, 2003.

[8] R. Olsson, I. Eriksson, J. Powell, A. Kaplan, "Advances in pulsed laser weld monitoring by the statistical analysis of reflected light", Opt. Lasers Eng. 49 (11), 1352-1359, 2011.

[9] G. Liu, X.-Y. Liu, and Q.-Y. Feng, "3D shape measurement of objects with high dynamic range of surface reflectivity", Appl. Opt., vol. 50, no. 23, pp. 4557–65, Aug. 2011.

[10] O. Detection, C. Of, O. Of, and D. Dimensions, "Optical detection and ranging characteristics of objects of different dimensions", vol. 55, no. 9, pp. 1012– 1018, 2012.

[11] Z. Yan, M. R. Anjum, and W. Xiaowei, "Influence Factor Analysis for 3D Imaging Laser Radar Range Profile", vol. 17, no. 2, pp. 142–147, 2013.

[12] H. Rapp, M. Frank, F. a. Hamprecht, and B. Jahne, "A theoretical and experimental investigation of the systematic errors and statistical uncertainties of Time-Of-Flight-cameras", Int. J. Intell. Syst. Technol. Appl., vol. 5, p. 402, 2008.

[13] R. I. Hartley and S. B. Kang, "Parameter-free radial distortion correction with centre of distortion estimation", Int'l Conf. Comput. Vision, Beijing, vol. 29, no. 8, pp. 1834–1841, 2005.

[14] R. D. Richmond and S. C. Cain, "Introduction to LADAR Systems," in Direct-detection LADAR systems, 2010, pp. 1–26.

[15] O. Steinvall, "Effects of target shape and reflection on laser radar cross sections.," Appl. Opt., vol. 39, no. 24, pp. 4381–91, Aug. 2000.

[16] J. Busck and H. Heiselberg, "Gated viewing and high-accuracy three-dimensional laser radar.," Appl. Opt., vol. 43, no. 24, pp. 4705–10, Aug. 2004.

[17] S. S. Patil and a. D. Shaligram, "On-line defect detection of aluminum coating using fiber optic sensor," Photonic Sensors, vol. 5, no. 1, pp. 72–78, 2015.

[18] G. V. Landon, Y. Lin, and W. B. Seales, "Towards automatic photometric correctionofcasuallyilluminateddocuments,"ComputerVisionandPatternRecognition, 2007. CVPR'07. IEEE Conference on, pp. 1–8, 2007.

[19] A. P. Pentland, "Finding the illuminant direction," JOSA, vol. 72, no. 4, pp. 448– 455, 1982.

[20] K. Hara and K. Nishino, "Variational estimation of inhomogeneous specular reflectanceandilluminationfromasingleview,"JOSAA,vol.28, no.2,pp.136–146, 2011.

[21] R.Hartley and S. B. Kang, "Parameter-freeradial distortion correctionwith center of distortion estimation," IEEE Trans. Pattern Anal. Mach. Intell., vol. 29, no. 8, pp. 1309–1321, 2007.

[22] Busck, J.; Heiselberg, H. Gated viewing and high-accuracy three-dimensional laser radar. Appl. Opt.215 2004, 43, 4705–10.

[23] Rostami, M.; Michailovich, O.; Wang, Z. Image Deblurring Using Derivative Compressed Sensing for Optical Imaging Application. IEEE Trans. Image Process. 2012, 21, 3139–3149.